Dollinger, Christoph ; Sorg, Michael ; Balaresque, Nicholas ; Fischer, Andreas

Measurement uncertainty of IR thermographic flow visualization measurements for transition detection on wind turbines in operation

Journal Article as: peer-reviewed accepted version (Postprint)

DOI of this document*(secondary publication): https://doi.org/10.26092/elib/3304

Publication date of this document: 13/09/2024

* for better findability or for reliable citation

Recommended Citation (primary publication/Version of Record) incl. DOI:

C. Dollinger, M. Sorg, N. Balaresque, A. Fischer,
Measurement uncertainty of IR thermographic flow visualization measurements for transition detection on wind turbines in operation, Experimental Thermal and Fluid Science, Volume 97, 2018, Pages 279-289,
ISSN 0894-1777, https://doi.org/10.1016/j.expthermflusci.2018.04.025.

Measurement uncertainty of IR thermographic flow visualization measurements for transition detection on wind turbines in operation

C. Dollinger[a,*], M. Sorg[a], N. Balaresque[b], A. Fischer[a]

[a] University of Bremen, Bremen Institute for Metrology, Automation and Quality Science, Linzer Str. 13, 28359 Bremen, Germany
[b] Deutsche WindGuard Engineering GmbH, Überseering 7, 27580 Bremerhaven, Germany

ARTICLE INFO

Keywords:
Thermographic flow visualization
Laminar-turbulent transition
Boundary layer transition measurements
Transition detection
Measurement uncertainty
Uncertainty propagation
Wind energy
Wind turbine rotor blades

ABSTRACT

The application of thermographic flow visualization on wind turbines in operation differs from the well-established application in wind tunnel experiments. The necessary temperature difference between the rotor blade and the flow only relies on the absorbed solar radiation, which often leads to a low signal-to-noise ratio. Furthermore, a large distance of up to 400 m exists between the rotor blade and the thermographic camera for ground based measurements, mainly due to the height of the wind turbine. This results in a poor spatial resolution as well as a small numerical aperture, which means a small detectable radiant power further degrades the signal-to-noise ratio. In order to determine the limits of measurability for the localization of the laminar-turbulent transition, the fundamental effects on the measurement uncertainty are investigated. For this purpose, the measurement uncertainty budgets for three signal processing algorithms are derived and validated with wind tunnel experiments and field measurements on a 1.5 MW wind turbine under sunny and cloudy weather conditions. As a result, the achievable standard uncertainty of the laminar-turbulent transition position for a temperature difference of 2 K amounts to 0.16 pixels in this case, which corresponds to 0.17% chord length. In addition, the measurement uncertainty is currently not limited by the measurement system (detector noise and fixed pattern noise of the camera), but by flow induced temperature fluctuations and fluctuations of the laminar-turbulent transition position itself. Hence, the field measurements on wind turbines in operation are still limited by the flow characteristics, i.e., the measurement object itself. Finally, one of the presented signal processing methods allows a robust, automated flow characterization for wind turbines in operation with subpixel accuracy in all of the presented measurements.

1. Introduction

In addition to numerical flow simulations and wind tunnel measurements, flow measurements on wind turbines in real operation conditions are essential for the development and the aerodynamic optimization of wind turbine rotor blades. For example, an early laminar-turbulent transition in the boundary layer of a rotor blade causes an increase in drag due to a higher skin friction [40], and an undesired and unnoticed separation of the boundary layer results in a sudden decrease in lift and a strong increase in pressure drag [18]. Both leads to a reduced performance of the wind turbine and, thus, reduces the energy yield. Furthermore, flow separations induce unsteady loads and vibrations [34], which negatively affect the durability of the whole wind turbine and increase the acoustic emissions of the rotor blades [49]. For this purpose, a contact-less and non-invasive measurement method for the visualization and the characterization of the boundary layer flow on wind turbine rotor blades in operation is required.

State-of-the-art methods for the boundary layer flow visualization on wind turbine rotor blades in operation generally involve the preparation of the rotor blade surface with tufts [45,48] or with an oil-pigment solution [17,31]. For the visualization of regions with separated flow so-called stall flags are used [8], which have to be mounted on the rotor blade surface. In addition, surface pressure measurements with pressure taps and microphones [4,2,39] or hot film measurements [38] are possible, though these methods are invasive to the rotor blade surface. The preparation of the rotor blade is time consuming and the precise positioning of the equipment is a costly process, as a turbine stop and the ascent by rope access technicians or the use of a work platform is necessary. Furthermore, the aforementioned approaches are invasive to the flow and, thus, have an influence on the boundary layer to be measured.

In contrast, thermographic measurements enable a non-invasive and fast measurement of the boundary layer state at the wind turbine in operation [13,47]. Thermographic flow measurements are an

* Corresponding author.
E-mail address: c.dollinger@bimaq.de (C. Dollinger).

established method for the visualization of different flow regimes in the boundary layer in wind tunnel experiments. With the existence of an initial temperature difference between the aerodynamic body and the fluid, the surface temperature of the aerodynamic body depends on the local heat transfer between the rotor blade and the flow, which is proportional to the skin friction in different flow regimes [35,11,22]. Initially used in supersonic flows [46,7], with advances in the measurement technology the thermographic flow visualization has also proved to be a suitable tool in subsonic flows [3,43].

Typical wind tunnel applications are the localization of the laminar-turbulent transition [21,25], the identification of laminar separation bubbles [32,37] or the visualization of a turbulent separation [22,20,14]. Recently, the automated detection of the laminar-turbulent transition was proposed by Crawford et al. [10] and by Joseph et al. [28] in order to gain also quantitative information, e.g., within long lasting wind tunnel campaigns. To increase sensitivity, wherever applicable, the aerodynamic body is usually externally or internally heated [6,5,11,12,1] or the fluid flow is cooled [21,23,42]. By that it is possible to cause the necessary temperature difference between the flow and the measured body surface. For the thermographic detection of the laminar-turbulent transition, heating power levels between several hundred [28] up to a few thousand [30,44] $\mathrm{W\,m^{-2}}$ are reported. Due to the thermal inertia of the surface, dynamic measurements are particularly challenging and part of current research [19,36].

Examples for successful transfers of the thermographic flow visualization from the laboratory to the area of operation can be found for in-flight experiments within the space shuttle program and for aircraft wings [33,9] as well as for measurements on rotating helicopter blades [27,30] and on wind turbines in operation [15,47]. Published measurements on wind turbines in operation have so far been primarily qualitative in nature. In contrast to measurements in wind tunnel experiments with controlled conditions, field measurements on wind turbines in operation face a number of additional challenges. Without the ability of an additional heating of the rotor blade surface, the available thermal contrast between the rotor blade and the flow only relies on the absorbed solar radiation, which leads to a low signal-to-noise-ratio. In addition, the dimensions and especially the height of a wind turbine lead to a large distance of up to 400 m between the thermographic camera and the rotor blade for ground based measurements. The large distance generally results in a poor spatial resolution and a small numerical aperture. Furthermore, the fast movement of the rotor blade with maximum tip speeds between 80 and 90 $\mathrm{m\,s^{-1}}$ [24,26] aggravate the localization of the laminar-turbulent transition. Until now, the limits of measurability for the thermographic localization of the laminar-turbulent transition are not determined and the fundamental effects on the measurement uncertainty for field measurements at wind turbines blades in operation are not identified. Furthermore there is a need for a robust evaluation method for field measurements, that is not dependent on a priori knowledge in terms of the position of the laminar-turbulent transition.

For this reason, an advanced evaluation algorithm for the localization of the laminar-turbulent transition in measurements on wind turbines in operation is introduced. The robust algorithm enables the localization of the laminar-turbulent transition with subpixel accuracy, even in ground based measurements on wind turbines in operation with a large measuring distance. Beyond that, a fundamental study of the achievable measurement uncertainty in field measurements is presented, e.g., the large distance and the low thermal contrast, are shown and their influence discussed. The analytic derivation of the measurement uncertainty is verified by Monte Carlo simulations and validated by wind tunnel experiments as well as field measurements on a 1.5 MW wind turbine for different weather conditions.

First the measurement approach is explained and three different evaluation methods for the localization of the laminar-turbulent transition in thermographic images are presented in Section 2. The experimental setup for the conducted wind tunnel experiments on the one hand and the conducted field measurements on the other hand is described in Section 3. The estimation of the resulting measurement uncertainty is derived in Section 4 and is validated by measurement results presented in Section 5. The article closes with conclusions and an outlook in Section 6.

2. Measurement approach

With the objective of a fast and non-invasive visualization of the boundary layer flow on wind turbine rotor blades, thermographic measurements in wind tunnel experiments and fields measurements at the wind turbine in operation were performed. In this section the principle of the thermographic flow visualization is explained and demonstrated on a sample image. In addition three different evaluation methods for the localization of the laminar-turbulent transition are presented.

2.1. Principle

The underlying principle for the thermographic flow visualization is that different flow regimes can be distinguished by their surface temperature, that differs due to a change in the local heat transfer coefficient affected by the flow regime characteristics. Hence, the same temperature difference between fluid and model surface will then cause different surface temperatures. Fig. 1 shows an example for a thermographic image of a rotor blade segment of a wind turbine in operation. Because of the absorbed solar radiation, the rotor blade surface is warmer than the flow. Due to this temperature difference, the surface areas with a laminar boundary layer flow are warmer than surface areas with a turbulent boundary layer flow, due to a lower heat transfer coefficient. Hence, the transition between the laminar and the turbulent flow regimes can be identified by a steep change in temperature.

The temperature change in the transition region can be used for an evaluation method for the localization of the laminar-turbulent transition. Crawford et al. [10] propose an extensive low pass filtering and averaging followed by a Sobel edge detection for the localization of the transition front. In Dollinger et al. [16] and Joseph et al. [28] an automated evaluation method in wind tunnel experiments based on the gradient of the temperature profile in flow direction is presented. In field measurements, the geometrical resolution is often low in the order of >10 mm per pixel due to the large working distances. For that reason an evaluation algorithm for the localization of the laminar-turbulent transition with a subpixel accuracy is required. In this work the favored signal processing method is based on the approximation of the temperature profile with a Gaussian cumulative distribution function, which results, as an interpolation is performed, in a subpixel accuracy. In Fig. 2 the temperature profile $T(y)$ and its gradient $\mathrm{d}T/\mathrm{d}y$ in flow direction are shown for the position $x = 500$ pixel, cf. Fig. 1. The steep

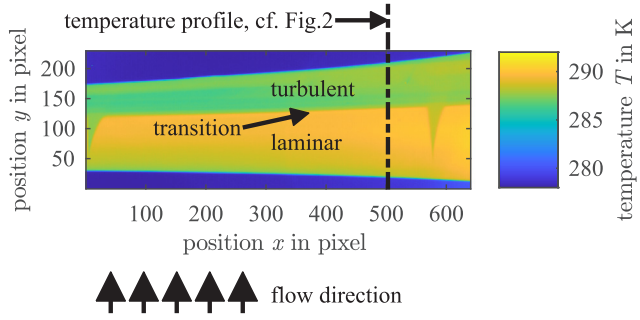

Fig. 1. Example of a thermographic image of the surface of a wind turbine rotor blade in operation. The relative flow direction is upwards and the laminar and the turbulent flow regimes are indicated as well as the laminar-turbulent transition. The two turbulence wedges are premature laminar-turbulent transitions due to contamination or imperfections on the rotor blade surface.

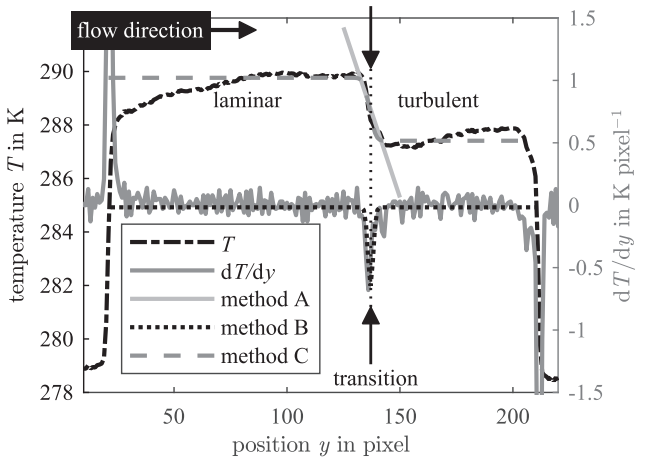

Fig. 2. Temperature profile $T(y)$ and its gradient $\mathrm{d}T/\mathrm{d}y$ in flow direction for the position $x = 500$ pixel, cf. Fig. 1. Furthermore, the result of the linear regression of the measured temperatures determined with method A, the non-linear regression of the temperature gradient with a Gaussian probability density function as in method B, and the nonlinear regression of the temperature profile with a Gaussian cumulative distribution function, hereafter referred to as method C, are shown.

change in temperature in the transition region results in a maximum of the absolute temperature gradient.

2.2. Evaluation methods

For the localization of the laminar-turbulent transition, three different evaluation algorithms A, B and C are introduced and compared in terms of achievable measurement uncertainty and the suitability for an robust, automated signal processing method. The results of the three approaches are indicated in Fig. 2.

Evaluation method A is based on a linear regression with the individual temperatures T_i at the discrete position y_i in the a priori known linear region of the laminar-turbulent transition. Using the regression results ($\hat{m}$ as slope and $\hat{n}$ as offset of the linear function) as well as an a priori defined temperature threshold $T_{\mathrm{threshold}}$, the y-position of the transition is obtained with the relation

$$y_{\mathrm{threshold}} = \frac{T_{\mathrm{threshold}} - \hat{n}}{\hat{m}} \tag{1}$$

with

$$\hat{m} = \frac{N\sum_{i=1}^{N} y_i T_i - \sum_{i=1}^{N} y_i \sum_{i=1}^{N} T_i}{\sum_{i=1}^{N} y_i^2 - \left(\sum_{i=1}^{N} y_i\right)^2}, \tag{2}$$

and

$$\hat{n} = \frac{\sum_{i=1}^{N} y_i^2 \sum_{i=1}^{N} T_i - \sum_{i=1}^{N} y_i \sum_{i=1}^{N} y_i T_i}{\sum_{i=1}^{N} y_i^2 - \left(\sum_{i=1}^{N} y_i\right)^2}, \tag{3}$$

whereas N is the number of measured temperature values T_i in the linear transition region y_i. The simple implementation of this algorithm is offset by the disadvantage of the manual determination of the position of the transition region and the value of the temperature threshold. For this reason a more robust evaluation method that can be used for an automation of the localization of the laminar-turbulent transition is presented with method B.

Method B is based on a nonlinear regression of the temperature gradient of the measured temperature profile on the rotor blade surface by a Gaussian probability density function (PDF) with a least squares method (LSM). The temperature gradient $\mathrm{d}T$ is the temperature difference between adjacent pixels with the width of one pixel $\mathrm{d}y$. The function for the fit is given by

$$\widetilde{T}' = \widetilde{a}\,\mathrm{e}^{-\left(\frac{\widetilde{y}-\widetilde{b}}{\sqrt{2}\,\widetilde{c}}\right)^2} + \widetilde{d}, \tag{4}$$

with the fit parameters $\widetilde{a}$ for the maximum height, $\widetilde{b}$ for the position of the maximum height as the transition position, $\widetilde{c}$ for the standard deviation (transition width parameter), and $\widetilde{d}$ for the offset of the Gaussian PDF. For the localization of the laminar-turbulent transition, the position $\widetilde{b}$ of the maximum of the Gaussian PDF that marks the position of the highest temperature gradient is defined as the laminar-turbulent transition position $\widetilde{y}_{\mathrm{tr}}$.

The third method C is based on the approximation of the measured temperature profile T_i with a Gaussian cumulative distribution function. The Gaussian cumulative distribution function is the integrated Gaussian probability density function. The model's function is given by:

$$\hat{T} = \hat{a}\ \mathrm{erf}\left(\frac{y-\hat{b}}{\sqrt{2}\ \hat{c}}\right) + \hat{d}. \tag{5}$$

The approximation parameters are, as in the case of the Gaussian probability density function, the maximum height $\hat{a}$, the y-position of the turning point $\hat{b} = y_{\mathrm{tr}}$, the width, i.e. the standard deviation, $\hat{c}$ and the offset $\hat{d}$. The result of this approach is as the results of the other two approaches depicted in Fig. 2. Analog to the approximation of the Gaussian probability density function, the approximation parameter $\hat{b}$ can be assumed as the position of the laminar-turbulent transition y_{tr}.

Method B and method C with the approximation of the temperature gradient by the Gaussian PDF and the approximation of the temperature profile by the Gaussian cumulative distribution function are advantageous, because, except for the positions of the leading edge and the trailing edge of the rotor blade, no additional information is required. Furthermore the fit algorithms are self-centering at the position of the laminar-turbulent transition. As a result both evaluating algorithm enable an robust, automated approach of the localization of the laminar-turbulent transition.

3. Experimental setup

Experimental measurements with a thermographic measurement system were performed in wind tunnel experiments and in field measurements on a wind turbine in operation. The thermographic measurement system and both of the experimental setups are presented in the following subsections.

3.1. Thermographic measurement system

A thermographic camera with a global shutter (snap-shot detector) is used from the manufacturer InfraTec. The detector is a cooled InSb focal plane array with a format of 640 × 512 pixels (model ImageIR 8300). The pixel size in the sensor plane amounts to 15 µm. Full-frame resolution images can be acquired at up to 100 Hz sampling frequency. The camera is sensitive between 2 and 5 µm and the noise equivalent temperature difference (NETD) is less than 25 mK @ 30 °C. The dynamic range is 14 bit and the integration time for the acquisition of an image can be set between 1 and 20,000 µs. The camera can be equipped with different lenses to fit the specific requirements of the measuring task. The camera is calibrated by the manufacturer in a standard calibration routine with measurements of a black body radiator at different temperatures. For the presented measurements a one point non-uniformity correction is performed before each of the measurements. The presented temperatures are therefore relative temperatures, and do not correspond to the absolute surface temperature of the rotor blade.

The thermographic images are acquired with the camera software development kit (SDK) from the camera manufacturer. It provides an

interface to MATLAB, which is used for the subsequent processing of the images, as described in Section 2.

3.2. Wind tunnel experiments

The wind tunnel experiments took place in Deutsche WindGuard's aero-acoustic wind tunnel in Bremerhaven, which is a closed-return type. The wind tunnel provides laminar flows (turbulence intensity <0.3%) at wind speeds of up to 100 m s^{-1} and for models with 0.9 m chord, Reynolds numbers of up to 6.0×10^6 can be achieved. The wind tunnel is operated with a closed test section. The closed test section allows testing of up to 0.9 m chord models, therefore wind turbine airfoil segments (2D) as well as winglets can be tested at or close to a 1:1 scale. In the measurements presented here, no additional heating is installed for the wind tunnel experiments. The necessary temperature difference for the thermographic flow visualization is only based on friction in the wind tunnel system and the subsequent increase of the flow temperature. For that reason, the reachable temperature difference between the laminar and the turbulent boundary layer flow regimes are relatively small ($\leqslant$ 1 K).

The aerodynamic airfoil model surface for the wind tunnel experiments is made of glass-fiber reinforced plastic (GFRP) with a polyurethane top coat as it is typical for rotor blades of wind turbines. In contrast to wind turbine rotor blades the inner structure of the aerodynamic model consists of a steel and aluminum frame. For the geometry of the airfoil model, a rotor blade from a wind turbine of the same type as the one presented in the field measurements, was geometrically measured at 5 radial positions using a laser scanning device. The resulting 2D geometry for the model is originally located at a radial position of 30.15 m and the total rotor radius amounts to 38.5 m. The model is scaled down from 1266 mm original chord-length to 800 mm to fit into the wind tunnel. The thickness relative to the chord-length of the model is 17%. The model is mounted vertically between two turntables in the wind tunnel.

For the wind tunnel measurements, the camera is equipped with a 12 mm wide-angle lens with an angular aperture of 44° × 36°. This results in an instantaneous field of view (IFOV) of 1.25 mrad for the given detector size. The thermographic camera observes the airfoil model in the wind tunnel test section through a CaF_2 (calcium fluoride) window with more than 90% transmission in the spectral sensitivity range of the camera. With a viewing distance of approximately 1.375 m between the camera and the aerodynamic model in the test section follows that 1.7 mm in the frame of the measurement object are represented by one pixel of the camera's detector. This results in a lateral resolution of 0.2% relative to the chord-length of the airfoil model.

3.3. Field measurements

The field measurements were conducted on a wind turbine GE 1.5 sl from the manufacturer General Electric. The wind turbine has a rated power of 1.5 MW, and the rotor blades made by the supplier LM Wind Power have a length of 37.3 m. The hub height of the wind turbine is 62 m. Fig. 3 shows the measurement setup for the field measurements in a distance of 169 m behind the wind turbine tower base on the suction side of the rotor blades.

For the measurements on the wind turbine in operation, a 200 mm telephoto lens is used. The lens has an angular aperture of 2.7° × 2.2° and with the given detector size the instantaneous field of view (IFOV) results in 0.08 mrad. The thermographic field measurements are conducted with a working distance of 180 m for different environmental conditions resulting in different temperature gradients between the laminar and the turbulent flow regime. For the used 200 mm infrared-telephoto lens, the distance to the wind turbine rotor blade results in a spatial resolution of 14.4 mm corresponding to one pixel of the camera. The thermographic camera is triggered by an optical trigger for the measurements with the wind turbine in operation to enable the acquisition of an image every time one of the blades is passing the camera's field of view, which happens with a frequency in the 0.5–1 Hz range.

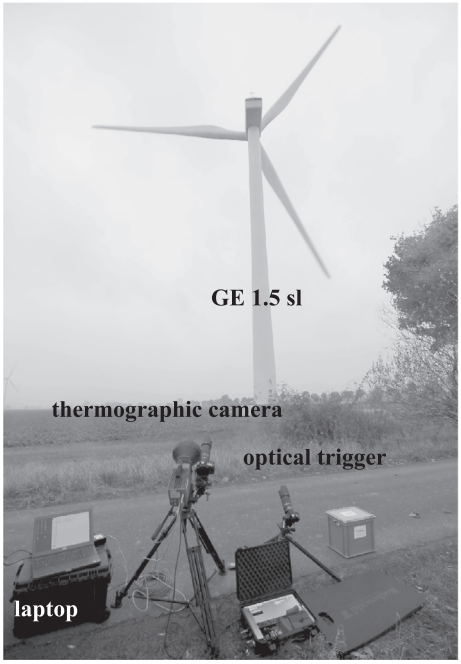

Fig. 3. Experimental setup for the field measurements at the wind turbine in operation. In the foreground the thermographic camera, an optical trigger and the laptop for the acquisition and evaluation of the images are shown. The wind turbine GE 1.5 sl is in the background at a distance of 169 m to the wind turbine tower base (working distance between rotor blade and camera: 180 m).

4. Measurement uncertainty estimation

In this section the achievable measurement uncertainty for the three signal processing methods A, B and C, introduced in Section 2.2, is estimated by Gaussian uncertainty propagations and verified by Monte Carlo simulations.

For the uncertainty of each individual temperature T_i per pixel measured with the thermographic camera, the detector noise and the fixed pattern noise are considered. Both, detector and fixed pattern noise were determined by a sequence of $L = 500$ measurements of a homogeneously tempered surface in a climate chamber at 293.15 K. The detector noise can be interpreted as the mean temporal noise of the temperature measurements:

$$\sigma_{T_{\text{detector}}} = \frac{1}{M \cdot N} \sum_{y=1}^{M} \sum_{x=1}^{N} \sqrt{\frac{1}{L-1} \sum_{l=1}^{L} (T_{yx}[l] - \overline{T}_{yx})^2} \tag{6}$$

with $\overline{T}_{yx} = \frac{1}{L} \sum_{l=1}^{L} T_{yx}[i]$ for the average temperature in the measurement sequence $T_{yx}[l]$, $l = 1, \ldots, L$ for each pixel $[y,x]$. Whereas $y = 1,\ldots,M$ stands for the image row and $x = 1,\ldots,N$ for the image column. The measurement of the detector noise results in $\sigma_{T_{\text{detector}}} = 0.033$ K.

The fixed pattern noise within the image due to the non-uniformity of the individual pixels can be quantified by a temporal averaging of the measurement sequence and a subsequent evaluation of the spatial noise:

$$\sigma_{T_{\text{pattern}}} = \sqrt{\frac{1}{(M \cdot N) - 1} \sum_{y=1}^{M} \sum_{x=1}^{N} (\overline{T}_{yx} - \overline{T})^2} \tag{7}$$

with the overall mean temperature $\overline{T} = \frac{1}{M \cdot N} \sum_{y=1}^{M} \sum_{x=1}^{N} \overline{T}_{yx}$. The fixed pattern noise measured after a non-uniformity correction is 0.009 K. The combined measurement uncertainty of the temperature results in $\sigma_{T_i} = \sqrt{\sigma^2_{T_i,\text{detector}} + \sigma^2_{T_{\text{pattern}}}} = 0.034$ K at a temperature of 293.15 K.

As the measured temperatures T_i in the thermographic image differ

in the range of a few Kelvin, the influence of the temperature-dependent photon shot noise is of interest for a measurement uncertainty estimation. According to Seitz [41] the photon statistics for multi-mode thermal light can be described by a Poisson distribution. The variance of the number $N_{i,\mathrm{photon}}$ of emitted photons is therefore given by the mean number of photons:

$$\sigma^2_{N_{i,\mathrm{photon}}} = \mathrm{Var}(N_{i,\mathrm{photon}}) = \overline{N}_{i,\mathrm{photon}}. \tag{8}$$

The mean number $\overline{N}_{i,\mathrm{photon}}$ of emitted photons can be calculated by applying Planck's law with the specific parameters of the camera and the measurement setup. The result is a function of the mean surface temperature $\overline{T}$ and is given by

$$\overline{N}_{i,\mathrm{photon}} = \sin^2(\alpha)\,\mathrm{d}A\,\mathrm{d}t \int_{\lambda_1}^{\lambda_2} \frac{2\pi c}{\lambda^4} \frac{1}{e^{\frac{hc_n}{\lambda k \overline{T}}}-1}\,\mathrm{d}\lambda, \tag{9}$$

where h is the Planck constant, c_n is the speed of light and k is the Boltzmann constant. For the specific measurement arrangement, the aperture angle α, the observed area $\mathrm{d}A$, the integration time $\mathrm{d}t$ and the detected wavelength range from λ_1 to λ_2 are inserted into Eq. (9). Applying an error propagation calculation to the inverse of the function g from Eq. (9) and inserting Eq. (8) yields the measurement uncertainty of each measured temperature value due to the photon shot noise:

$$\sigma_{T_{i,\mathrm{shot}}} = \sqrt{\left(\frac{\partial g^{-1}}{\partial N_{i,\mathrm{photon}}}\bigg|_{N_{i,\mathrm{photon}}=\overline{N}_{i,\mathrm{photon}}}\right)^2 \overline{N}_{i,\mathrm{photon}}}\,. \tag{10}$$

The uncertainty of the temperature due to photon shot noise is in the range from 0.016 K to 0.008 K for measurement object surface temperatures between 273.15 K and 333.15 K, which corresponds to the calibration range of the presented camera. At 293.15 K the photon shot noise is 0.012 K. The influence of the photon shot noise to the overall uncertainty σ_{T_i} of the temperature can be estimated by a calculation of the remaining noise components by $\sqrt{\sigma^2_{T_i} - \sigma^2_{T_{i,\mathrm{photon}}}} = 0.032$ K. As a result, the temperature uncertainty is not dominated by photon shot noise and is therefore neglected in the following considerations.

4.1. Linear regression of the temperature profile (method A)

Inserting Eqs. (2) and (3) in Eq. (1) and applying an uncertainty propagation results in the uncertainty of the transition position for the evaluation method A:

$$\sigma_{y_{\mathrm{threshold}}} = \sqrt{\sum_{i=1}^{N} \left(\frac{\partial y_{\mathrm{threshold}}}{\partial T_i}\right)^2 \sigma^2_{T_i}}. \tag{11}$$

Due to the negligible influence of the photon shot noise, the same value for the uncertainty σ_{T_i} of each temperature value T_i is applied for the uncertainty estimation. For this purpose the mean temperature of the temperature profile is taken into account to calculate the shot noise component. Fig. 4 shows the calculated uncertainty of the laminar-turbulent transition position as a function of the total temperature difference ΔT in the transition region for different temperature uncertainties. The transition region is assumed to be 12 pixels wide, whereas for the linear regression only the nearly linear part of 6 pixels width is used, and the total temperature difference ΔT of the temperature profile is varied between 0.1 K and 10 K. The solid line represents the uncertainty of the position of the laminar-turbulent transition for an experimental setup for field measurements with a measurement distance of 180 m, a mean surface temperature of 293.15 K and the camera equipped with the telephoto lens as described in Section 3. Furthermore, the result of a Monte Carlo simulation with 10,000 runs for each total temperature difference with a temperature uncertainty $\sigma_T = 0.034$ K is shown in Fig. 4. At very low temperature differences below 0.2 K the Monte Carlo simulation results begin to differ from the estimation due to the non-linearity of the temperature

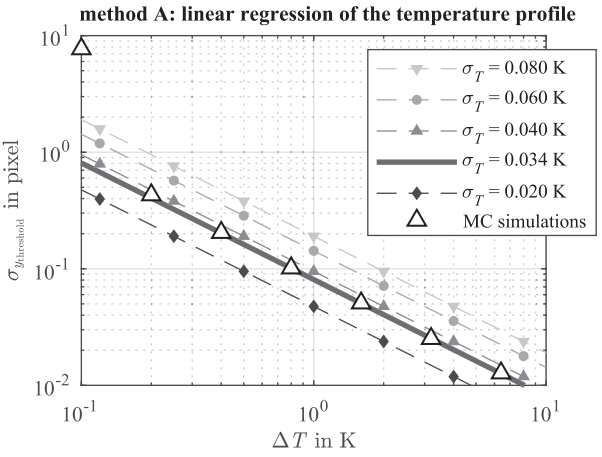

Fig. 4. Calculated uncertainty of the transition position for method A as a function of the total temperature difference ΔT in the transition region with an assumed width of 12 pixels for different temperature uncertainties. For the linear regression only the nearly linear part of the temperature profile is used, which is 6 pixels wide. The solid line represents the calculation for the presented experimental setup for field measurements, which is verified by Monte Carlo (MC) simulations indicated by white triangles.

profile and the low signal-to-noise ratio. For temperature differences $\geqslant 0.2$ K the estimated measurement uncertainty is in a good agreement with the simulations.

4.2. Approximation of the temperature gradient (method B)

In method B with the approximation of the temperature gradient by a Gaussian PDF, the laminar-turbulent transition position $\widetilde{y}_{\mathrm{tr}}$ is defined as the maximum of the fit function that marks the position of the highest temperature gradient. The uncertainty of the transition position equals the uncertainty of the estimated model parameter $\widetilde{b}$:

$$\sigma_{\widetilde{y}_{\mathrm{tr}}} = \sqrt{\mathrm{Var}(\widetilde{b})}. \tag{12}$$

Therefore the measurement uncertainty can be determined by calculating the covariance matrix of the estimator $\underline{\widehat{\theta}}_{\widetilde{T}'} = [\widetilde{a},\widetilde{b},\widetilde{c},\widetilde{d}]^T$ that is based on the fit function $\widetilde{T}'$, cf. Eq. (4). As a result of an uncertainty propagation calculation applied to the least squares estimator the covariance matrix reads [29]:

$$\mathrm{Cov}(\underline{\widehat{\theta}}_{\widetilde{T}'}, \underline{\widehat{\theta}}_{\widetilde{T}'}) = (H^{\mathrm{T}}_{\widetilde{T}'} H_{\widetilde{T}'})^{-1} H^{\mathrm{T}}_{\widetilde{T}'} C_{\mathrm{d}T_{\widetilde{i}}}\, H_{\widetilde{T}'} (H^{\mathrm{T}}_{\widetilde{T}'} H_{\widetilde{T}'})^{-1}, \tag{13}$$

whereas $H_{\widetilde{T}'}$ is the Jacobian matrix with the partial derivatives of the fit function for each fit parameter of $\underline{\widehat{\theta}}_{\widetilde{T}'}$ in each position $\widetilde{y}_i$ of the temperature gradient,

$$H_{\widetilde{T}'} = \begin{bmatrix} \frac{\partial \widetilde{T}'}{\partial \widetilde{a}}\Big|_{\widetilde{y}_{i=1}} & \frac{\partial \widetilde{T}'}{\partial \widetilde{b}}\Big|_{\widetilde{y}_{i=1}} & \frac{\partial \widetilde{T}'}{\partial \widetilde{c}}\Big|_{\widetilde{y}_{i=1}} & \frac{\partial \widetilde{T}'}{\partial \widetilde{d}}\Big|_{\widetilde{y}_{i=1}} \\ \vdots & \vdots & \vdots & \vdots \\ \frac{\partial \widetilde{T}'}{\partial \widetilde{a}}\Big|_{\widetilde{y}_{i=N-1}} & \frac{\partial \widetilde{T}'}{\partial \widetilde{b}}\Big|_{\widetilde{y}_{i=N-1}} & \frac{\partial \widetilde{T}'}{\partial \widetilde{c}}\Big|_{\widetilde{y}_{i=N-1}} & \frac{\partial \widetilde{T}'}{\partial \widetilde{d}}\Big|_{\widetilde{y}_{i=N-1}} \end{bmatrix}, \tag{14}$$

and $C_{\mathrm{d}T_{\widetilde{i}}}$ is the covariance matrix of the temperature differences $\mathrm{d}T_i = T_i - T_{i-1}$ between adjacent pixels. Assuming that the uncertainty of each temperature value amounts to σ_T, elementary calculations lead to the covariance matrix

$$C_{\mathrm{d}T_{\widetilde{i}}} = \begin{bmatrix} 2\sigma_T^2 & -\sigma_T^2 & 0 & \dots & 0 \\ -\sigma_T^2 & 2\sigma_T^2 & -\sigma_T^2 & \dots & 0 \\ 0 & -\sigma_T^2 & 2\sigma_T^2 & \dots & 0 \\ \vdots & \vdots & \vdots & \ddots & \vdots \\ 0 & \dots & 0 & -\sigma_T^2 & 2\sigma_T^2 \end{bmatrix}. \tag{15}$$

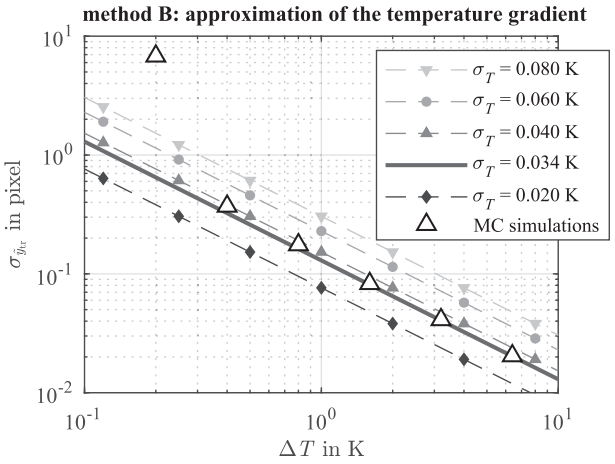

Fig. 5. Calculated measurement uncertainty of the transition position for method B as a function of the total temperature difference ΔT in the transition region with an assumed width of 12 pixels ($\pm\, 4\tilde{c}$) for different temperature uncertainties. The solid line represents the calculation for the presented experimental setup for field measurements, which is verified by Monte Carlo (MC) simulations indicated by white triangles.

Note that the covariances between the temperature gradient values are not taken into account for the non-weighted least squares estimation, so that the resulting estimator is suboptimal according to the Gauss-Markov theorem.

The result of the uncertainty estimation for the signal processing method B with Gaussian fitting is shown in Fig. 5 for different temperature uncertainties σ_T. As a result, the estimated measurement uncertainties for method A and method B are indirectly proportional to the total temperature difference of the temperature profile when the transition width remains constant. In a similar manner to Fig. 4, the solid line in Fig. 5 represents the uncertainty $\sigma_{\hat{y}_{tr}}$ of the position of the laminar-turbulent transition for the presented experimental setup for the field measurements, and the results for the Monte Carlo simulation are marked with white triangles. Again the transition region is assumed to be 12 pixels ($\pm\, 4\tilde{c}$, cf. Eq. (4)) wide and the total temperature difference of the temperature profile is varied between 0.1 K and 10 K. The results of the uncertainty propagation begin to differ from the Monte Carlo simulation results for low total temperature differences below 0.4 K, which is due to the non-linearity of the temperature profile and the low signal-to-noise ratio. However, for temperature differences $\geqslant$ 0.4 K the uncertainty estimation is verified and thus applicable.

In comparison to the linear regression method A, the measurement uncertainty of the laminar-turbulent transition is 60% higher with the approximation of the temperature gradient method B. An uncertainty of the temperature of 0.034 K at a total temperature difference of $\Delta T = 1$ K in the 12 pixel wide transition region results in an uncertainty of the transition position of 0.081 pixels for the linear regression (method A) and in 0.130 pixels for the approximation of the gradient by a Gaussian PDF (method B). The worse performance of method B can be explained by the non-consideration of the correlation of the adjacent temperature gradients in the signal processing algorithm of the Gaussian fitting (non-weighted least squares estimation). When using a weighted least squares estimator, the achievable measurement uncertainty can be reduced to 0.091 pixels. Another way to overcome this disadvantage of method B is to avoid the temperature gradient for the evaluation. For this reason, a nonlinear approximation of the temperature profile is proposed in the next subsection.

4.3. Approximation of the temperature profile (method C)

Method C is the approximation of the temperature profile with the Gaussian cumulative distribution function, cf. Eq. (5). By that, the calculation of the temperature gradient can be avoided and no covariances between the adjacent values of the temperature gradient have to be considered. However, the advantages of the approximation of the Gaussian probability density function in terms of an automation of the signal processing remain. Analog to the approximation of the Gaussian PDF, the parameter $\hat{b}$ of the fit function can be assumed as the position of the laminar-turbulent transition y_{tr}. The uncertainty of the position is thus determined according to:

$$\sigma_{y_{tr}} = \sqrt{\mathrm{Var}(\hat{b})}. \tag{16}$$

This relationship again enables the estimation of the measurement uncertainty of the position of the laminar-turbulent transition by calculating the estimator's covariance matrix [29]:

$$\mathrm{Cov}(\underline{\hat{\theta}}_{\hat{T}}, \underline{\hat{\theta}}_{\hat{T}}) = (H_{\hat{T}}^{\mathrm{T}}\ C_{T_{\tilde{i}}}^{-1}\ H_{\hat{T}})^{-1}. \tag{17}$$

The Jacobian matrix of the approximation function is

$$H_{\hat{T}} = \begin{bmatrix} \frac{\partial \hat{T}}{\partial \hat{a}}\Big|_{y_{\tilde{i}}=1} & \frac{\partial \hat{T}}{\partial \hat{b}}\Big|_{y_{\tilde{i}}=1} & \frac{\partial \hat{T}}{\partial \hat{c}}\Big|_{y_{\tilde{i}}=1} & \frac{\partial \hat{T}}{\partial \hat{d}}\Big|_{y_{\tilde{i}}=1} \\ \vdots & \vdots & \vdots & \vdots \\ \frac{\partial \hat{T}}{\partial \hat{a}}\Big|_{y_{\tilde{i}}=N} & \frac{\partial \hat{T}}{\partial \hat{b}}\Big|_{y_{\tilde{i}}=N} & \frac{\partial \hat{T}}{\partial \hat{c}}\Big|_{y_{\tilde{i}}=N} & \frac{\partial \hat{T}}{\partial \hat{d}}\Big|_{y_{\tilde{i}}=N} \end{bmatrix}. \tag{18}$$

Due to the absence of covariance between the individual values of the temperature profile, the covariance matrix $C_{T_{\tilde{i}}}$ is a diagonal matrix whose main diagonal is represented by the variance $\sigma_{T_{\tilde{i}}}^2$ of the temperature $T_{\tilde{i}}$:

$$C_{T_{\tilde{i}}} = \begin{bmatrix} \sigma_T^2 & 0 & \dots & 0 \\ 0 & \sigma_T^2 & \dots & \vdots \\ \vdots & \vdots & \ddots & 0 \\ 0 & \dots & 0 & \sigma_T^2 \end{bmatrix}. \tag{19}$$

The result of the uncertainty estimation for the approximation of the temperature profile with the Gaussian cumulative distribution function is shown in Fig. 6. The width of the transition region, the underlying uncertainty and the temperature difference ΔT do not differ from Figs. 4 and 5. The estimated measurement uncertainty for the approximation of the temperature profile by the Gaussian cumulative distribution function also shows the dependence $\sigma_{y_{\mathrm{threshold}}} \sim \frac{1}{\Delta T}$. For this approach for $\Delta T = 0.1$ K, the uncertainty estimation only deviate slightly from the Monte Carlo simulations indicated by the white

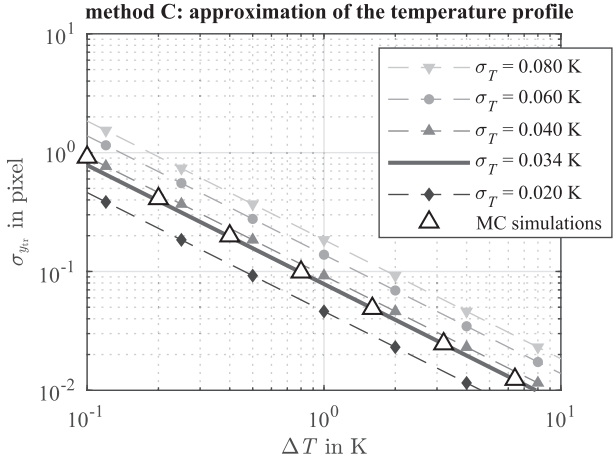

Fig. 6. Calculated uncertainty of the transition position for the approximation of the temperature profile method C as a function of the total temperature difference ΔT in the transition region with an assumed width of 12 pixels ($\pm\, 4\hat{c}$) for different temperature uncertainties. The solid line represents the calculation for the presented experimental setup for field measurements, which is verified by Monte Carlo (MC) simulations indicated by white triangles.

triangles. Therefore, this estimation can be considered as verified for $\Delta T \geqslant 0.1$ K.

A temperature difference of $\Delta T = 1$ K and a transition region with a width of 12 pixels results in a uncertainty of the transition position of 0.078 pixels for the given uncertainty of the temperature $\sigma_T = 0.034$ K. Under the assumed conditions, this result is even better than the result of the linear regression method A. However, in contrast to method A, the approximation of the temperature gradient does not rely on a priori knowledge as the position of the transition region or the temperature threshold. Without the a priori knowledge, method A fails for an automated approach for the localization of the laminar-turbulent transition. The approximation of the temperature gradient also requires no a priori knowledge, but results in a 67% higher measurement uncertainty compared to method C. For this reason the approximation of the temperature profile by a Gaussian cumulative distribution function with its ability of a self-centering at the transition position and the low measurement uncertainty is to favor for an robust, automated signal processing algorithm.

5. Measurement results

For the validation of the measurement uncertainty estimation an evaluation with all three signal processing algorithms is applied to wind tunnel measurement data as well as to field measurements on the wind turbine in operation at different environmental conditions.

5.1. Wind tunnel experiments

The wind tunnel experiment is conducted at a chord-Reynolds number of 3.0×10^6 which corresponds to a wind speed in the wind tunnel test section of $56\,\mathrm{m\,s^{-1}}$. Fig. 7(a) to Fig. 7(c) show the airfoil model in the wind tunnel with an angle of attack of 5° and flow from left to right evaluated with each of the three evaluation methods A, B and C. The strong radial distortion as a consequence of the use of the 12 mm wide-angle lens is corrected by a camera calibration according to Zhang [50]. The measured total temperature difference ΔT between the surface area with the laminar and the surface area with the turbulent boundary layer is 0.6 K and the width of the transition region is 24 pixels. The applied linear regression of the temperature profile method A is depicted in Fig. 7(a). Due to the constant temperature threshold $T_{\mathrm{threshold}}$, a surface temperature drop at position $x = 200$ causes a systematic error, i.e. a shift in the transition position for $x \geqslant 200$. For this reason, the quantification of the measured position and the standard deviation of the laminar-turbulent transition position is carried out for $x < 200$. The laminar-turbulent transition position $y_{\mathrm{threshold}}$ is evaluated for 200 x-positions in the thermographic image and results in 312.20 pixels in the image. The measured standard uncertainty of the transition position is 0.58 pixels, which corresponds to 1.21 mm on the airfoil model chord. The measurement uncertainty relative to the chord-length c is ± 0.12%. Note that the systematic behavior of the transition position along the x-axis is determined with a parabolic regression and subtracted from the measured positions when determining the standard deviation. The correction of the systematic behavior is applied to all subsequent measurements. The measured uncertainty is about a factor of 3 above the estimated measurement uncertainty, that is 0.2 pixels. In addition to the remaining position uncertainty of 0.09 pixels after the calibration, to some extent this can be explained by local flow induced temperature fluctuations. The measured standard deviation of the temperature in the region of the laminar-turbulent transition is 0.07 K, which is significantly higher than the noise sources considered in Section 4. An uncertainty propagation with the higher temperature uncertainty leads to an estimated position uncertainty of the laminar-turbulent transition of 0.41 pixels.

In contrast to method A, the approximation of the temperature gradient by a Gaussian PDF is insensitive to the surface temperature drop at position $x = 200$, which demonstrates the higher robustness of

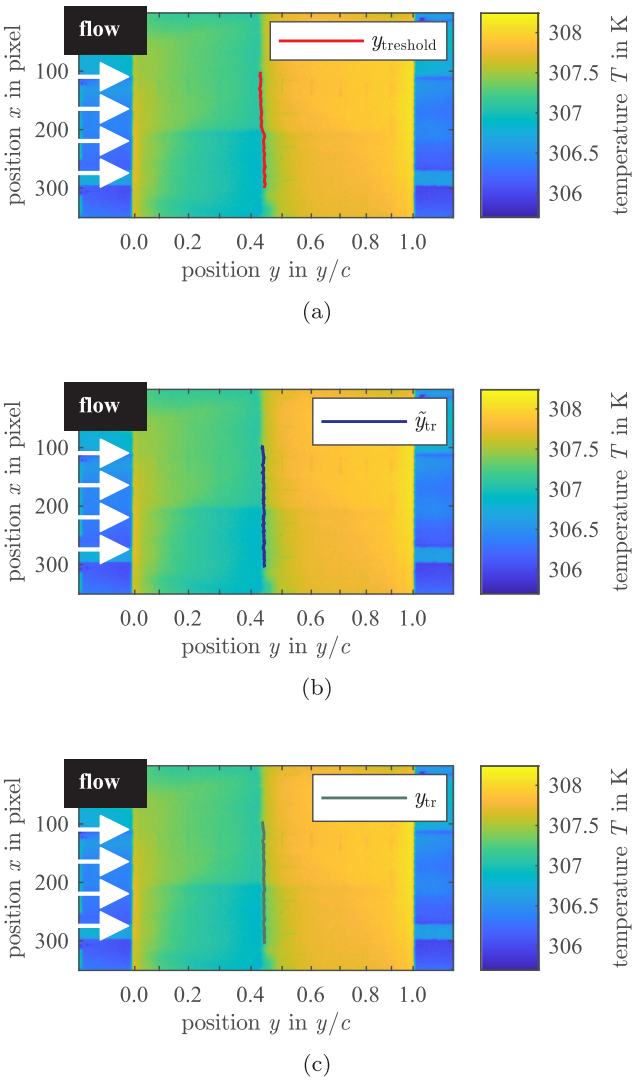

Fig. 7. Thermographic measurement of the aerodynamic airfoil model in the wind tunnel section evaluated with (a) the linear regression of the temperature profile method A, (b) the approximation of the temperature gradient by a Gaussian PDF method B and (c) the approximation of the temperature profile by a Gaussian cumulative distribution function method C. The laminar-turbulent transition position is evaluated for 200 x-positions in the thermographic image. The transition position $y_{\mathrm{threshold}}$ evaluated with method A is 312.20 ± 0.58 pixels. The transition position $\tilde{y}_{\mathrm{tr}}$ evaluated with method B is 315.43 ± 0.77 pixels. An evaluation with method C results in a transition position of 315.63 ± 0.56 pixels.

this evaluation method, cf. Fig. 7(b). The mean position of the laminar-turbulent transition is 315.43 pixels for method B. Under the prevailing circumstances, the measured standard uncertainty of the transition position $\tilde{y}_{\mathrm{tr}}$ with method B is 0.77 pixels or 1.30 mm, respectively, which is about a factor of 2.5 higher than the uncertainty estimation, i.e., 0.32 pixels. The uncertainty propagation with the measured standard uncertainty of the temperature in the transition region (0.07 K) results in 0.65 pixels.

As already expected by the measurement uncertainty estimation, the approximation of the temperature profile by a Gaussian cumulative distribution function combines the advantages of the two signal processing approaches discussed above. The result of the third approach method C is shown in Fig. 7(c). The measured position of the laminar-turbulent transition is 315.63 pixels with a standard uncertainty of 0.56 pixels. Based on the measurement uncertainty estimation with a temperature difference of $\Delta T = 0.6$ K, the width of the transition area of 24 pixels and the uncertainty of the temperature $\sigma_T = 0.034$ K, a

Table 1
Measurement uncertainty of the laminar-turbulent transition location in consideration of different influences. The results refer to the wind tunnel measurement shown in Fig. 10 with a measured temperature difference of $\Delta T = 0.6$ K between the laminar and the turbulent boundary layer flow regime and a 24 pixels wide transition region.

influence	uncertainty in pixel		
	method A $\sigma_{y_{\text{threshold}}}$	method B $\sigma_{\tilde{y}_{\text{tr}}}$	method C $\sigma_{y_{\text{tr}}}$
noise of the IR camera	0.20	0.32	0.19
camera calibration	0.09	0.09	0.09
flow induced temperature fluctuations	0.35	0.56	0.32
fluctuations of the transition position	0.41	0.41	0.41
measured standard uncertainty	0.58	0.77	0.56

measurement uncertainty of the position of 0.19 pixels would have been expected. However, the estimation does not take into account the influence of the calibration and the flow-induced temperature fluctuations. The uncertainty propagation with the measured standard uncertainty of 0.07 K results in an uncertainty of the transition position of 0.38 pixels.

For all three methods the assumed origin of the remaining difference between the measured and the estimated measurement uncertainty are natural fluctuations of the laminar-turbulent transition position due to the flow turbulence or imperfections of the airfoil surface. Hence, the flow induced temperature fluctuations limit the achievable measurement uncertainty. The results for all three signal processing algorithms are summarized in Table 1.

With the knowledge of the airfoil model geometry, the angle of attack and the angle of view of the camera, the position in the image can be transformed to the position on the model surface relative to the chord length, which results in for method C $y_{\text{tr}}/c = 0.44$.

5.2. Field measurements

The field measurements are performed at two different environmental conditions, resulting in different temperature gradients between the laminar and the turbulent boundary layer flow regime. The presented field measurements are both performed at 10 rpm of the rotor, resulting in 0.5 Hz rotor blade pass frequency. In combination with the chosen integration time of 1600 µs this causes a motion blur of 3.5 pixels at the radial position of the region of interest at $r = 30.15$ m. Due to the motion blur, the transition region is wider, which is considered in the uncertainty calculations.

Fig. 8 shows a thermographic measurement of the rotor blade of the GE 1.5 sl wind turbine made with 5 individual thermographic images. In this measurement situation, the direct solar radiation was heating the rotor blade surface (sunny weather condition), resulting in a measured temperature difference of $\Delta T = 2$ K between the laminar and the turbulent boundary layer flow regime. The radial rotor position is indicated on the abscissa. Note that it appears as if the transition occurs uniformly at about half the chord. This is due to the two-dimensional imaging of the three-dimensional rotor blade. By considering the geometry and the twist angle of the rotor blade, a significant variation of the transition position can be observed. A strong radial gradient in transition position can be noticed at the tip of the rotor blade. The 2D airfoil section measured in the wind tunnel experiment is located at 30.15 m. The thermographic image of the rotor blade area between the rotor radius of 29 and 31 m is depicted in Fig. 9. The results for all three evaluation methods A to C are shown in individual subfigures. The results of both evaluating methods for the evaluation of this field measurement are shown in Table 2.

In contrast to the estimated uncertainty $\sigma_T = 0.034$ K of the temperature due to detector noise and fixed pattern noise of the camera, the standard deviation of the temperature in the region of the laminar-turbulent transition is 0.09 K due to additional temperature fluctuations induced by the flow. In combination with a real variation of the laminar-turbulent transition position due to locally different flow conditions and surface imperfections of the rotor blade, the resulting measurement uncertainty is not dominated by noise from the measurement system but by the fluid flow, i.e., the measurement object itself. As a result, the localization of the laminar-turbulent transition in the thermographic flow visualization image is possible with a standard uncertainty of 0.16 pixels, 0.21 pixels or 0.16 pixels with method A, B and C, respectively. This corresponds to 0.18%, 0.24% and 0.18% of the chord length of the rotor blade section.

Knowing the geometry of the rotor blade in the region of the evaluated section as well as the twist angle and the pitch angle of the blade allows the projection and transformation of coordinates in order to obtain the transition position on the rotor blade surface relative to the chord length $y_{\text{tr}}/c = 0.42$. In comparison with the y_{tr}/c-position in the wind tunnel experiment ($y_{\text{tr}}/c = 0.44$), this result is in a good agreement.

Fig. 10 shows the result for a field measurement with a measured temperature difference of 1 K between the laminar and the turbulent boundary layer flow regime. For this measurement day there was no direct solar radiation but only indirect radiation through a cloud cover (cloudy weather condition). Again the results for all three methods are depicted in the subfigures Fig. 10(a)–(c). Because of a series of turbulent wedges as a result of surface contamination or imperfections of the rotor blade surface the radial position for the evaluation area is moved to a nearby region without turbulence wedges. The obvious difference of the laminar-turbulent transition position is due to the fact that the thermographic image was taken with a 180° change in rotational angle of the rotor with the rotor blade on its way up, which due to the blade twist angle, pitch angle, and observer location, effectively changes the viewing angle considerably. For presentation purposes the image is rotated to match Figs. 8 and 9. The measurement uncertainty budged for this measurement is shown in Table 3.

The standard uncertainty of the temperature in the region of the transition is 0.04 K. However, the lower total temperature difference of

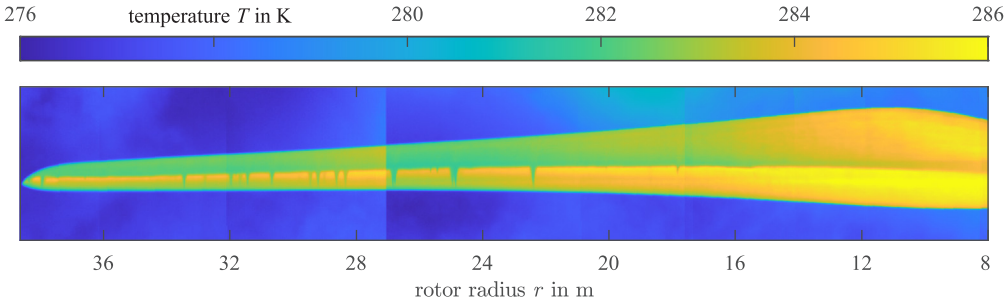

Fig. 8. Thermographic measurement of the suction side of the rotor blade of the GE 1.5 sl wind turbine. 5 individual images were taken from 180 m working distance and subsequently merged.

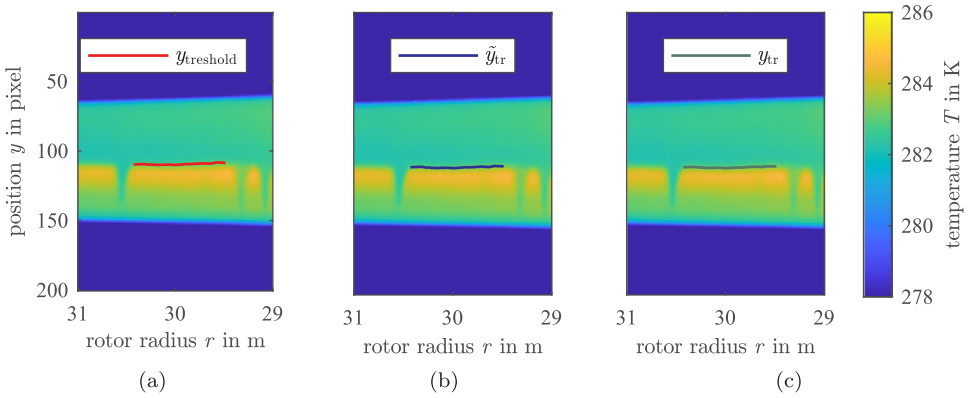

Fig. 9. Thermographic measurement of the rotor blade section corresponding to the geometry of the airfoil model measured in the wind tunnel. The measured temperature difference between the flow regimes is 2 K (sunny weather condition). The laminar-turbulent transition position is evaluated for 67 y-positions in the thermographic image. (a) The transition position evaluated with method A is $y_{\text{threshold}} = 109.88 \pm 0.16$ pixels. (b) The transition position evaluated with method B is $\tilde{y}_{\text{tr}} = 110.10 \pm 0.21$ pixels. (c) An evaluation with method C results in a transition position of $y_{\text{tr}} = 110.14 \pm 0.16$ pixels.

Table 2
Measurement uncertainty of the laminar-turbulent transition location in consideration of different influences. The results refer to the field measurement shown in Fig. 9 with a measured temperature difference of $\Delta T = 2$ K (sunny weather condition) between the laminar and the turbulent boundary layer flow regime and a 12 pixels wide transition region.

influence	uncertainty in pixel		
	method A $\sigma_{y_{\text{threshold}}}$	method B $\sigma_{\tilde{y}_{\text{tr}}}$	method C $\sigma_{y_{\text{tr}}}$
noise of the IR camera	0.04	0.07	0.04
flow induced temperature fluctuations	0.10	0.16	0.09
fluctuations of the transition position	0.12	0.12	0.12
measured standard uncertainty	0.16	0.21	0.16

Table 3
Measurement uncertainty of the laminar-turbulent transition location in consideration of different influences. The results refer to the field measurement shown in Fig. 7 with a measured temperature difference of $\Delta T = 1$ K (cloudy weather condition) between the laminar and the turbulent boundary layer flow regime and a 16 pixels wide transition region.

influence	uncertainty in pixel		
	method A $\sigma_{y_{\text{threshold}}}$	method B $\sigma_{\tilde{y}_{\text{tr}}}$	method C $\sigma_{y_{\text{tr}}}$
noise of the IR camera	0.10	0.15	0.09
flow induced temperature fluctuations	0.08	0.13	0.07
fluctuations of the transition position	0.12	0.12	0.12
measured standard uncertainty	0.17	0.23	0.17

the temperature profile leads to a slightly increased measurement uncertainty of the laminar-turbulent transition position. The uncertainty budget for all three evaluation methods is summarized in Table 3. As a result the standard uncertainty of the measurement for the approximation of the temperature profile by a Gaussian distribution function (method C) amounts to 0.17 pixels, which corresponds to 0.19% of the associated chord length c. The result for method A is also 0.17 pixel (0.19% c) and the result for method B is 0.23 pixel (0.26% c), respectively. Hence, the measurement uncertainty for the cloudy weather condition ($\Delta T = 1$ K) is increased only by 6% (method C) compared to the sunny weather condition ($\Delta T = 2$ K). This is due to lower flow induced temperature fluctuations, which, due to the thermal inertia of the rotor blade surface, are not as pronounced as at a lower temperature difference.

6. Conclusions

Thermographic flow visualization measurements were performed in order to develop an robust, automated signal processing algorithm for the localization of the laminar-turbulent transition in field measurements on wind turbines in operation. For three signal processing methods, based on a linear regression of the transition region (method A), an approximation of the temperature gradient by a Gaussian probability density function (method B) and the approximation of the temperature profile by a Gaussian cumulative distribution function, the achievable measurement uncertainty is estimated with an uncertainty propagation calculation verified by Monte Carlo simulations. A wind tunnel experiment as well as field measurements of a 1.5 MW wind turbine were performed for the validation of the evaluation methods.

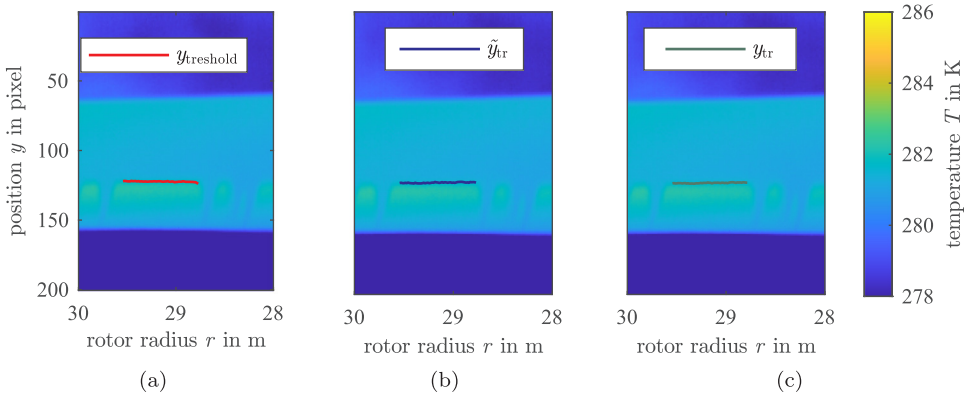

Fig. 10. Thermographic measurement of the rotor blade section at $r = 30.15$ m, corresponding to the geometry of the aerodynamic airfoil model measured in the wind tunnel. The measured temperature difference between the flow regimes is 1 K (cloudy weather condition). The laminar-turbulent transition position is evaluated for 55 x-positions in the thermographic image. The transition position evaluated with method A is $y_{\text{threshold}} = 121.83 \pm 0.17$ pixels and the transition position evaluated with method B is $\tilde{y}_{\text{tr}} = 121.39 \pm 0.23$ pixels. The approximation of the temperature profile with a Gaussian distribution function method C results in the transition position $y_{\text{tr}} = 121.58 \pm 0.17$ pixels.

All methods enable a localization of the transition position with sub-pixel accuracy for temperature differences $\geqslant 1$ K between the laminar and the turbulent boundary layer flow regime.

Even though the estimated measurement uncertainty as well as the measured standard uncertainty of an evaluation with the linear regression method A are lower than for the non-weighted Gaussian fitting method B, the method B is more suitable for an automated evaluation algorithm. The application of method A requires the a priori knowledge of the position of the transition region and a chosen temperature threshold, whereas method B requires none. As a result, the signal processing method B is more robust with respect to artifacts in the thermographic images. Due to the non-consideration of the correlation of the adjacent temperature gradient values in the signal processing algorithm of the non-weighted least squares estimation, the measurement uncertainty for method B is significantly higher than for the linear regression method A. For this reason, the non-linear approximation of the temperature profile with a Gaussian cumulative distribution function (method C) is proposed for the robust, automatic evaluation of the transition position, as it combines the advantages of the other two algorithms.

The evaluation of the field measurements show, that the laminar-turbulent transition can be located from a working distance of 180 m with a standard uncertainty of 0.17% relative to the rotor blade chord length, which here corresponds to 0.16 pixels. The temperature difference under sunny weather conditions was 2 K between the laminar and the turbulent boundary layer flow regime. The measurement uncertainty is not limited due to noise from the measurement system but due to the measurement object, i.e., the boundary layer flow characteristics. Additionally, the temperature difference between the flow regimes in the transition region as well as the width of the transition region affect the accuracy of the localization significantly.

Future investigations will involve the evaluation of thermographic flow visualization measurements on wind turbine rotor blades in order to study the influence of leading edge contamination and erosion (both causing an early laminar-turbulent transition) on the performance of the wind turbine.

Acknowledgements

The financial support by the German Federal Environmental Foundation (Grant No. 27118) and the Bremerhaven Economic Development Company with a funding of the State of Bremen (Grant No. 59203) is gratefully acknowledged. The authors also thank Infratec GmbH for the practical support during the experiments.

References

[1] P. Bæk, P. Fuglsang, Experimental detection of transition on wind turbine airfoils, in: Proceedings of the European Wind Energy Conference and Exhibition, 2009, pp. 1628–1652.
[2] C. Bak, H. Aagaard Madsen, U. Schmidt Paulsen, M. Gaunaa, P. Fuglsang, J. Romblad, N.A. Olesen, P. Enevoldsen, J. Laursen, L. Jensen, DAN-AERO MW: detailed aerodynamic measurements on a full scale MW wind turbine, in: 2010 European Wind Energy Conference and Exhibition, 2010.
[3] A.-M. Bouchardy, G. Durand, Processing of infrared thermal images for aerodynamic research, in: Proceedings of SPIIE, Applications of Digital Image Processing, vol. 0397, 1983, pp. 0397–0397-6.
[4] C.P. Butterfield, M.D. Jenks, D.A. Simms, W.P. Musial, Aerodynamic pressure measurements on a rotating wind turbine blade, in: 36th Instrument Society of America International Instrumentation Symposium, 1990.
[5] G.M. Carlomagno, L. de Luca, Infrared thermography in heat transfer, in: W.I. Yang (Ed.), Handbook of Flow Visualization, Hemisphere Publishing Corporation, 1989, pp. 531–553 (Chapter 32).
[6] G.M. Carlomagno, L. de Luca, G. Buresti, G. Lombardi, Characterization of boundary layer conditions in wind tunnel tests through infrared thermography imaging, in: Proceedings of SPIE, Applications of Infrared Technology, vol. 918, 1988.
[7] D.L. Compton, Use of an infrared-imaging camera to obtain convective heating distributions, AIAA J. 10 (8) (1972) 1130–1132.
[8] G.P. Corten, H.F. Veldkamp, Insects can halve wind-turbine power, Nature 412 (2001) 41.
[9] B.K. Crawford, G.T. Duncan, D.E. West, W.S. Saric, Quantitative boundary-layer transition measurements using IR thermography, AIAA SciTech (2014) 13–17.
[10] B.K. Crawford, G.T. Duncan, D.E. West, W.S. Saric, Robust, automated processing of ir thermography for quantitative boundary-layer transition measurements, Exp. Fluids 56 (7) (2015) 149.
[11] L. de Luca, G.M. Carlomagno, G. Buresti, Boundary layer diagnostics by means of an infrared scanning radiometer, Exp. Fluids 9 (3) (1990) 121–128.
[12] L. de Luca, G. Guglieri, G. Cardone, G.M. Carlomagno, Experimental analysis of surface flow on a delta wing by infrared thermography, AIAA J. 33 (8) (1995) 1510–1512.
[13] C. Dollinger, N. Balaresque, M. Sorg, Thermographic boundary layer visualisation of wind turbine rotorblades in operation, in: Europe's Premier Wind Energy Event, Barcelona. European Wind Energy Association, EWEA, 2014.
[14] C. Dollinger, N. Balaresque, M. Sorg, A. Fischer, {IR} thermographic visualization of flow separation in applications with low thermal contrast, Infrared Phys. Technol. 88 (2018) 254–264.
[15] C. Dollinger, N. Balaresque, M. Sorg, G. Goch, Thermographic measurement method for turbulence boundary layer analysis on wind turbine airfoils, in: Wind Power Conference and Exhibition, Las Vegas. American Wind Energy Association, AWEA, 2014.
[16] C. Dollinger, M. Sorg, P. Thiemann, Aeroacoustic optimization of wind turbine airfoils by combining thermographic and acoustic measurement data, Dewi Magazin 43 (2013) 61–64.
[17] D.M. Eggleston, K. Starcher, A comparative study of the aerodynamics of several wind turbines using flow visualization, J. Sol. Energy Eng. 112 (4) (1990) 301–309.
[18] M. Gad-el Hak, D.M. Bushnell, Separation control: review, J. Fluids Eng. 113 (1) (1991) 5–30.
[19] A.D. Gardner, C. Eder, C.C. Wolf, M. Raffel, Analysis of differential infrared thermography for boundary layer transition detection, Exp. Fluids 58 (9) (2017) 122.
[20] A.D. Gardner, C.C. Wolf, M. Raffel, A new method of dynamic and static stall detection using infrared thermography, Exp. Fluids 57 (9) (2016) 149.
[21] E. Gartenberg, W.G. Johnson, R.E. Wright, D.L. Carraway, C.B. Johnson, Boundary-layer transition-detection in a cryogenic wind tunnel using infrared imaging, AIAA J. 30 (2) (1992) 444–446.
[22] E. Gartenberg, A.S. Roberts, Airfoil transition and separation studies using an infrared imaging system, J. Aircraft 28 (4) (1991) 225–230.
[23] E. Gartenberg, R.E. Wright, Boundary-layer transition detection with infrared imaging emphasizing cryogenic applications, AIAA J. 32 (9) (1994) 1875–1882.
[24] R. Gasch, J. Twele, Wind Power Plants, Springer, Nature, 2012.
[25] M. Grawunder, R. Reß, C. Breitsamter, Thermographic transition detection for low-speed wind-tunnel experiments, AIAA J. 54 (6) (2016) 2012–2016.
[26] E. Hau, Wind Turbines: Fundamentals, Technologies, Application, Economics, Springer, Nature, 2013.
[27] J.T. Heineck, E. Schülein, M. Raffel, Boundary layer transition detection on a rotor blade using rotating mirror thermography, in: 5th American Helicopter Society Decennial Specialist Meeting, Aeromechanics, San Francisco 2014, 2014.
[28] L.A. Joseph, A. Borgoltz, W. Devenport, Infrared thermography for detection of laminar-turbulent transition in low-speed wind tunnel testing, Exp. Fluids 57 (5) (2016) 77.
[29] S.M. Kay, Fundamentals of Statistical Signal Processing, Prentice Hall Signal Processing Series, Prentice Hall PTR, Upper Saddle River, NJ, 1993.
[30] W. Lang, A.D. Gardner, S. Mariappan, C. Klein, M. Raffel, Boundary-layer transition on a rotor blade measured by temperature-sensitive paint, thermal imaging and image derotation, Exp. Fluids 56 (6) (2015) 118.
[31] P. Medina, S. Schreck, J. Johansen, L. Fingersh, Oil-flow visualization on a SWT-2.3-101 wind turbine, in: 29th AIAA Applied Aerodynamics Conference, American Institute of Aeronautics and Astronautics (AIAA), 2011.
[32] S. Montelpare, R. Ricci, A thermographic method to evaluate the local boundary layer separation phenomena on aerodynamic bodies operating at low reynolds number, Int. J. Therm. Sci. 43 (3) (2004) 315–329.
[33] W. Nitsche, J. Szodruch, Laminar-flow instrumentation for wind-tunnel and flight experiments, J. Aircraft 30 (2) (1993) 192–200.
[34] A. Pellegrino, C. Meskell, Vortex shedding from a wind turbine blade section at high angles of attack, J. Wind Eng. Ind. Aerodyn. 121 (2013) 131–137.
[35] A. Quast, Detection of transition by infrared image techniques, in: 12th International Congress on Instrumentation in Aerospace Simulation Facilities (ICIASF 87), Williamsburg 1987, 1987.
[36] M. Raffel, A.D. Gardner, T. Schwermer, C.B. Merz, A. Weiss, J. Braukmann, C.C. Wolf, Rotating blade stall maps measured by differential infrared thermography, AIAA J. (2017).
[37] R. Ricci, S. Montelpare, E. Silvi, Study of acoustic disturbances effect on laminar separation bubble by IR thermography, Exp. Therm. Fluid Sci. 31 (4) (2007) 349–359.
[38] A.P. Schaffarczyk, D. Schwab, M. Breuer, Experimental detection of laminar-turbulent transition on a rotating wind turbine blade in the free atmosphere, Wind Energy 20 (2) (2017) 211–220.
[39] A.P. Schaffarczyk, D. Schwab, S. Ingwersen, M. Breuer, Pressure and hot-film measurements on a wind turbine blade operating in the atmosphere, J. Phys.: Conf. Ser. 555 (1) (2014) 012092.
[40] H. Schlichting, Boundary-layer theory, McGraw-Hill Series in Mechanical Engineering, seventh ed., McGraw-Hill, New York, 1979.
[41] P. Seitz, Photon-noise limited distance resolution of optical metrology methods, in: Optical Measurement Systems for Industrial Inspection, vol. 6616, 2007, 66160D-1.
[42] A. Séraudie, J. Perraud, F. Moens, Transition measurement and analysis on a swept wing in high lift configuration, Aerosp. Sci. Technol. 7 (8) (2003) 569–576.
[43] G.S. Settles, Modern developments in flow visualization, AIAA J. 24 (8) (1986)

1313–1323.
[44] B. Simon, A. Filius, C. Tropea, S. Grundmann, IR thermography for dynamic detection of laminar-turbulent transition, Exp. Fluids 57 (5) (2016) 93.
[45] N. Swytink-Binnema, D.A. Johnson, Novel image analysis method for blade aerodynamic performance on operational turbine, J. Phys: Conf. Ser. 524 (1) (2014) 012016.
[46] H. Thomann, B. Frisk, Measurement of heat transfer with an infrared camera, Int. J. Heat Mass Transf. 11 (5) (1968) 819–826.
[47] D. Traphan, P. Meinlschmidt, F. Schlüter, O. Lutz, J. Peinke, G. Gülker, High-speed measurements of different laminar-turbulent transition phenomena on rotor blades by means of infrared thermography and stereoscopic PIV, in: Proceedings of the 10th Pacific Symposium on Flow Visualization and Image Processing, Neapel, 2015.
[48] S. Vey, H.M. Lang, C.N. Nayeri, C.O. Paschereit, G. Pechlivanoglou, Extracting quantitative data from tuft flow visualizations on utility scale wind turbines, J. Phys: Conf. Ser. 524 (1) (2014) 012011.
[49] S. Wagner, R. Bareiss, G. Guidati, Wind Turbine Noise, Springer-Verlag, Berlin, Heidelberg, 1996.
[50] Z. Zhang, A flexible new technique for camera calibration, IEEE Trans. Pattern Anal. Mach. Intell. 22 (11) (2000) 1330–1334.